

1 *5957 Revision 1*

2 **DIAGENETIC F-RICH FERROAN CALCITE AND ZIRCON IN THE OFFSHORE SCOTIAN**
3 **BASIN, EASTERN CANADA: SIGNIFICANCE FOR UNDERSTANDING THERMAL**
4 **EVOLUTION OF THE BASIN**

5
6 Georgia Pe-Piper^{*}, Christopher Sangster, and Yuanyuan Zhang[†]

7
8 Department of Geology, Saint Mary's University, Halifax, Nova Scotia B3H 3C3, Canada
9

10

11

ABSTRACT

12

In the Scotian Basin, offshore eastern Canada, an unusual combination of high heat flow
13 in the Cretaceous and the abundance of halite has resulted in unusual diagenetic minerals such as
14 sphalerite. The Newburn H-23 well is the most distal well in the basin with good core samples
15 and has two previously unknown diagenetic mineral occurrences: fluorine-rich ferroan calcite
16 and diagenetic zircon. This study uses SEM backscattered electron images and EDS analyses,
17 EMP WDS mineral analyses and Raman spectroscopy to determine mineral chemistry and
18 textures in order to investigate the diagenetic and thermal significance of these minerals.

19

Late diagenetic Fe-calcite contains 1–2.5 wt% fluorine, mostly from adsorption, but
20 rarely as small fluorite crystals. Fluoride is also adsorbed on the surfaces of some framework
21 minerals and chlorite. Fluoride was transported in highly saline formation brines derived from
22 the Argo salt Formation. Zircon grains, 20–40 μm in size, have crystal outlines which are
23 straight adjacent to pores, partially lobate filling porosity, and cross cutting other grains: these
24 may be diagenetic. Some zoned detrital zircon grains show 1–3 μm wide diagenetic outgrowths.

25 Neof ormation of diagenetic zircon requires temperatures of $>250^{\circ}\text{C}$. Transport of zirconium is
26 favoured by ligands in low pH solution, principally fluoride and phosphate anions, with
27 zirconium mobilized during the alteration of metamict detrital zircon under low-grade
28 metamorphic conditions. The presence of diagenetic sphalerite and the documented mid
29 Cretaceous thermal event in the Scotian Basin indicate conditions that could have been suitable
30 for the formation of diagenetic zircon in this well. Suitable geological conditions for such
31 diagenetic formation of zircon will be found in a subsiding rift basin with early evaporites that is
32 affected by a subsequent phase of volcanism due to new rifting or subduction.

33

34 **Keywords:** diagenesis, zircon, ferroan calcite, fluorine, Scotian Basin

35

36

37 * E-mail: gpiper@smu.ca

38 † Present affiliation : School of Earth and Space Sciences, Peking University, Beijing, P.R .

39 China 100871.

40

INTRODUCTION

41 Diagenetic minerals preserve an important record of fluid flow and paleotemperatures in
42 the development of hydrocarbon basins. The Scotian Basin (Fig. 1) is a passive continental
43 margin basin with an unusual diagenetic history. Thick halite accumulated during Late Triassic
44 rifting (Holser et al. 1988), and as a consequence, formation waters in the basin are highly saline.
45 The Jurassic basin was located at the northeast end of the incipient Atlantic Ocean, and the
46 thermal effects of subsequent rifting between the Grand Banks and Iberia in the Cretaceous were
47 felt throughout the basin (Bowman et al. 2012). In the latest Jurassic and early Cretaceous, the
48 basin was a uniquely large depocenter on the eastern North American margin, accumulating
49 several kilometers of sandy deltaic sediment derived from the uplift of the Labrador rift (Zhang
50 et al. 2014). This sediment loading drove an active salt tectonic system (Albertz et al. 2010), with
51 salt detachments and extensional listric faulting providing pathways for diagenetic fluids (Pe-
52 Piper et al. 2015).

53 The unusual combination of high heat flow some 100 Ma after initial rifting of the basin,
54 and the abundance of halite in the basin has resulted in unusual diagenetic minerals in wells in
55 the more proximal parts of the basin on the Scotian Shelf, including sphalerite and Mn-rich
56 siderite (Pe-Piper et al. 2015). In this study, we investigate diagenesis in the only deep-water
57 well in the Scotian Basin with a long record of sandstone diagenesis in sidewall cores, the
58 Newburn H-23 well, drilled in 977 m water depth to a total depth of 6070 m. This well provides
59 the most basinward set of sandy core samples of any well in the Scotian basin. Therefore, as
60 diagenetic fluids originated the deep basin depocenter and migrated up-dip through the basin,
61 this well provides information about the early fluids. The purpose of this study was to investigate
62 diagenetic minerals in the most basinward setting possible. Particular attention is paid to two

63 diagenetic minerals, zircon and a fluorine-rich ferroan calcite (F-rich Fe-calcite), in order to
64 better understand the evolution of both temperature and diagenetic fluids in the basin.

65 REGIONAL GEOLOGICAL SETTING

66 The early stages of Triassic rifting in the Scotian basin produced syn-rift clastic
67 successions and salt deposits (Fig. 2). As rifting continued into the Jurassic, the deposition
68 became dominated by carbonate rocks. This was followed by fluvial, deltaic, and shelf
69 deposition of the sandstones and shales of the Upper Jurassic and Lower Cretaceous Missisauga
70 and Logan Canyon Formations (Wade and MacLean 1990), with principally shales and some
71 sandy turbidites in deep water. Later deposits in the Upper Cretaceous and Cenozoic are shales
72 and lesser chinks.

73 The Scotian Basin has been strongly influenced by salt tectonics (Albertz et al. 2010).
74 The Upper Triassic-(?) Lower Jurassic Argo Formation salt was remobilized, principally in the
75 Jurassic and Cretaceous, with widespread salt expulsion creating accommodation beneath the
76 Scotian Shelf (Cummings and Arnott 2005), when extensive allochthonous salt bodies were
77 emplaced on the Scotian Slope (Kendell 2012). The Newburn H-23 well is located in zone II of
78 Shimeld (2004), which is dominated by vertical salt structures, with autochthonous salt overlying
79 syn-rift clastic sedimentary rocks and Meguma terrane basement (Fig. 1b; Deptuck et al. 2009).

80 Basin modeling for the Scotian Basin (Williamson 1995; OETR 2011) suggests that most
81 maturation and hydrocarbon charge took place during the Cretaceous. Fluid inclusions show that
82 hydrocarbon transport postdated silica overgrowths and the main carbonate cements, but that
83 some secondary fluid inclusions in fractures contain hydrocarbons (Karim et al. 2012). In the
84 central Scotian Basin, the C-isotope composition of carbonate cements and fluid inclusions in
85 cements indicate a period of flow of hot (<175°C and <23 wt.% NaCl_{eq}) basinal brines in the

86 Aptian-Albian (Wierzbicki et al. 2006; Karim et al. 2012). At this time, regionally high heat flow
87 in the northern Appalachians that resulted in high vitrinite reflectance in the lower Cretaceous
88 Chaswood Formation on land and widespread paleomagnetic resetting of basement rocks
89 (Bowman et al. 2012). Barite and sphalerite are widespread late diagenetic minerals in deeply
90 buried sandstones.

91 In the Newburn H-23 well, thin sandstone and siltstone beds are present in the Albian
92 Cree Member of the Logan Canyon Formation, and the Barremian–Hauterivian Upper and
93 Middle Missisauga Formations (Fig. 3). These beds were interpreted as deep-water turbidites
94 prior to drilling, but biota (OETR 2011) and sedimentary structures indicate an outer shelf
95 depositional environment.

96 METHODS

97 Polished thin sections were made from rock slices from 21 sidewall cores, of which 12
98 had fine sandstone or siltstone layers and were studied in detail (Fig. 3). Diagenetic minerals
99 textures were studied from backscattered electron (BSE) images acquired by scanning electron
100 microscope (SEM), supplemented by elemental X-ray maps of selected features acquired by
101 SEM. Minerals were identified by energy dispersive spectroscopy (EDS) analysis using the
102 SEM, and wavelength dispersive spectroscopy (WDS) chemical analyses were obtained by
103 electron microprobe (EMP).

104 The SEM analysis was completed in the Regional Analytical Centre at Saint Mary's
105 University using a LEO 1450 VP SEM acquiring the BSE images and EDS chemical analyses of
106 minerals. This SEM has a maximum resolution of 3.5 nm at 30 kV. It is equipped with an INCA
107 X-max 80 mm² silicon-drift detector (SDD) EDS system that has a detection limit >0.1%. A
108 tungsten filament produces a 10 µm beam, calibrated with a cobalt standard. Elemental X-ray

109 mapping data were processed by the QuantMap package in Oxford Instrument's INCA program.
110 The color bar at the bottom of each elemental mapping image is scaled to EDS analysis (volatile
111 free) and values are presented as oxides to facilitate comparison with standards.

112 Minerals requiring fluorine analysis were analyzed at the Regional Electron Microprobe
113 Centre at Dalhousie University, using a JEOL-8200 electron microprobe with a Noran 133 eV
114 energy dispersive spectrometer and five wavelength spectrometers. Fluorite (~49 wt.% F) was
115 chosen as a standard for fluorine, with fluorapatite analyzed as a control, because SEM-EDS
116 analysis suggested fluorine contents as high as ~25 wt.%. Diffracting crystal LDE1 is more
117 sensitive than other crystals in the microprobe spectrometers and is thus chosen for F analysis.
118 The measured elements and different standards for calibration of each element and the element
119 distribution for each channel (spectrometer) with different diffracting crystal are listed in
120 Supplementary Table 1.

121 Raman laser (LRM) spectroscopy was completed in the Regional Analytical Centre at
122 Saint Mary's University using a Horiba Jobin-Yvon LabRam HR confocal instrument. The LRM
123 uses a 100mW 532 nm Nd-YAG diode laser from Toptica Photonics and a Synapse charge-
124 coupled device from Horiba Jobin-Yvon. The LRM also uses a 100x Olympus MPlanN objective
125 for images and analysis. The detector is cooled to -50 °C, and a minimal working distance
126 between the objective and sample is used to reduce interference. A 25 µm confocal hole
127 diameter, and 600 grooves/mm grating was used for all analyses, yielding a spectral resolution of
128 approximately 20 nm. Spectra were collected using an accumulation of three, ten second
129 acquisitions with a laser spot size of approximately 1 µm at 50% laser power. The spectra were
130 collected in two spectral windows 200-4000 cm⁻¹ and 200-2600 cm⁻¹. The analyzed polished thin
131 section had all carbon coating removed using methanol to increase the intensity of the peaks.

132

DATA PRESENTATION

133 **Fluorine-rich ferroan calcite**

134 Sandstone and siltstone layers show diagenetic minerals similar to those described
135 elsewhere in shallow water wells in the Scotian Basin (Karim et al. 2010; Gould et al. 2010; Pe-
136 Piper et al. 2015). Unusual diagenetic ferroan calcite (Fe-calcite) grains with elevated fluorine
137 content (2–27 wt.%) were identified using SEM EDS analyses in five samples. The term ferroan
138 calcite is applied to calcite with 1–6 mole % FeCO_3 ; magnesian calcite has 1–7 mole % MgCO_3 .
139 One sample with F-rich Fe-calcite was from the Cree Member (4353.5 m), the others from the
140 Middle Missisauga Formation (most common at 5403.6 m and 5407 m, also present at 5213.5 m
141 and 5408.5 m) (Supplementary Table 2). EDS analyses of F are imprecise, but in EMP analyses,
142 fluorine totals range between 1 wt.% and 2.5 wt.% in F-rich Fe-calcite. Fluorine was also found
143 in diagenetic chlorite with concentrations as high as 6.9 wt.%.

144 Textural evidence suggests that the F-rich Fe-calcite is a late diagenetic mineral.

145 Framework grains comprise quartz, lithic clasts, K-feldspar, albite and muscovite, together with
146 small amounts of volcanic glass. Quartz grains have overgrowths that have resulted in complete
147 silica cementation in many areas, but with some pores bounded by euhedral quartz crystal faces.
148 Calcite, Mg-calcite and Fe-calcite engulf originally detrital quartz and feldspar grains (Fig. 4A).
149 Fe-calcite and F-rich Fe-calcite engulf quartz overgrowths (Figs. 4C, 4D, and 4E positions a) and
150 Fe-calcite surrounds and replaces ankerite that may have replaced framework feldspar (Fig. 4C).
151 Earlier Mg-calcite and calcite are replaced by later F-rich Fe-calcite (Fig 4F) and Fe-calcite (Fig.
152 4B). Chlorite fills dissolution voids in F-rich Fe-calcite and calcite (Fig. 4F), cuts F-rich Fe-
153 calcite (Figs. 4D and 4E), and engulfs silt sized quartz (Fig. 4E). Late siderite forms rims (Fig.
154 4A) on or fills secondary dissolution voids (Fig. 4B) in Fe-calcite. It is associated with late

155 diagenetic sphalerite and barite (Fig. 3). The paragenetic sequence for the minerals which
156 interact with F-rich Fe-calcite is thus: quartz overgrowths → ankerite + calcite + Mg-calcite →
157 Fe-calcite + F-rich Fe-calcite → *dissolution* → fibrous chlorite → siderite ± sphalerite ± barite.

158 EMP data from a variety of diagenetic calcite grains show that the Mg content of Fe-
159 calcite increases steadily from 0.1 to 0.3 wt.% as Fe increases, whereas fluorine ranges from 0 up
160 to 2.5 wt.% in the Fe-calcite (Figs. 5A, 6A) and shows no correlation with Fe content (Fig. 5C).
161 There is no fluorine in the Mg-calcite and there is no correlation between Mg and fluorine in the
162 Fe-calcite (Fig. 5B), despite the relationship suggested by several studies that a higher Mg
163 content increases the adsorption of fluoride (F⁻) onto calcite (Rude and Aller 1991).

164 The question of how F⁻ is incorporated in calcite has been further investigated by Raman
165 spectroscopy. In the literature, both F⁻ adsorption and surface precipitation of fluorite on calcite
166 have been proposed (Budyanto et al., 2015). Raman spectral analyses were performed on F-rich
167 Fe-calcite crystals from sample 5403.6 m in order to determine if fluorine is present as fluorite
168 on the F-rich Fe-calcite surface (Supplementary Appendix 1). All of the analyses returned calcite
169 as the major mineral phase (Fig. 7), however two analyses, ~2 μm apart, showed minor peaks
170 which correspond to peaks from fluorite. When compared to the EMP analyses (Supplementary
171 Appendix 1, and Supplementary Table 3), no relationship was found between areas which have
172 high fluorine content and those areas which have fluorite spectral lines. This suggests that
173 fluorite surface precipitation probably occurred as patches in the F-rich Fe-calcite and was not
174 the only method by which fluorine was incorporated into the F-rich Fe-calcite analyses. Since no
175 fluorite peaks were found in the other analyzed grains, it seems that F⁻ adsorption onto Fe-calcite
176 was predominant, and the conditions which favored the surface precipitation of fluorite did not
177 persist throughout the entire period of formation of the F-rich Fe-calcite.

178 The question of how F⁻ is incorporated in calcite has been further investigated by
179 elemental mapping of a sandstone sample (5408.5 m) with F-rich Fe-calcite cement (Figs. 8 and
180 9). This was to determine if fluorite microcrystals can be seen; if minerals other than calcite were
181 hosts for fluorine; and if textural distribution of fluorine provides evidence for timing of F⁻
182 enrichment. The area mapped (Fig. 8A) has framework grains of quartz, albite and muscovite
183 and an apparently deformed lithic clast largely pseudomorphed by calcite and chlorite. This lithic
184 clast includes a few 5–10 μm quartz grains, a 40 μm long muscovite flake, a 10 μm grain of
185 titania, and (from EDS analysis) some phosphate. Most of the chlorite is fibrous or platy, with a
186 porous, diagenetic appearance (Fig. 8B). Secondary porosity has delicate chlorite fibers (Fig.
187 8B), suggesting that the porosity formed by volume reduction from a precursor, rather than by
188 dissolution of chlorite. The calcite appears sparry with abundant secondary porosity particularly
189 along crystal boundaries (Fig. 8C). The silica overgrowths partly engulf albite and show euhedral
190 faces against residual porosity. Some secondary porosity formed by dissolution along crystal
191 boundaries in the silicate mineral framework (position c in Fig. 8A).

192 In the lithic clast, fluorine is strongly positively correlated with the presence of calcite
193 (Figs. 9B and 9C). Lower abundances of fluorine are present in the chlorite. Morphologically
194 similar late chlorite in another sample with a similar lithic clast (Fig. 4E) also contains fluorine
195 (up to 3 wt. %). Fluorine is also present in the outermost few microns of the framework silicate
196 minerals (Fig. 9B, where the white line marks the edge of quartz and albite). In many cases,
197 especially in the albite, the high fluorine is related to the presence of secondary porosity, but this
198 is not the case in some of the silica overgrowths on the right side of the image (unless the
199 porosity is out of the plane of the thin section). The resolution of the elemental mapping is not
200 sufficient to distinguish between surface adsorption of F⁻ and surface precipitation of fluorite, but

201 no evidence has been seen for precipitation of fluorite, such as the presence of larger crystals of
202 fluorite in any of the samples. Furthermore, F^- is adsorbed onto chlorite and the margins of
203 framework quartz. In the case of chlorite (Fig. 8B), the F^- may be in the observed μm -scale
204 porosity, but image resolution is insufficient to determine if there is nano-scale porosity in the
205 quartz (Figs. 8A and 9D). We thus conclude that there is predominantly F^- adsorption rather than
206 fluorite precipitation.

207 **Diagenetic zircon**

208 The zircon grains from the Newburn H-23 well range in size from $\sim 20 \mu\text{m}$ to $\sim 40 \mu\text{m}$
209 (Fig. 10) and appear to be euhedral or subhedral and clean, with rare dissolution voids and
210 fractures. Crystal outlines in relationship to porosity may be straight (euhedral) (Figs. 10A, 10B,
211 10C, and 10F), partially lobate (Fig. 10F), appearing to partly fill porosity (Figs. 10A, 10B, and
212 10D), and cross cutting framework and cement minerals including chlorite (Figs. 10D and 10F),
213 calcite (Fig. 10B), kaolinite, K-feldspar, and quartz (Figs. 10D and 10H): such textures are
214 commonly present in late diagenetic minerals. On the other hand, at least some of the small
215 euhedral zircons could be detrital framework grains. High magnification images of some of such
216 zircon grains (Fig. 11) show outgrowths (Figs. 11A, 11B, and 11C), dissolution accompanied by
217 dark patches (Fig. 11D), and internal zoning of the main zircon crystal (Fig. 11A). This suggests
218 that although small euhedral zircon grains could be detrital, some have diagenetic outgrowths.
219 LA-ICPMS U-Pb dating of selected zircons was attempted, but no reliable data were obtained
220 because of the small size of the grains and the low content of radiogenic products, indicating a
221 Late Mesozoic age or younger.

222

DISCUSSION

223 **F-rich Fe calcite**

224 The F-rich Fe-calcite is common in the deeper studied samples, late in their paragenesis,
225 and seems to be associated with dissolution, fibrous chlorite lining secondary porosity and late
226 siderite. These observation suggest that the origin of the fluorine enrichment is related to deep
227 burial diagenetic processes.

228 Fluorine tends to concentrate in aragonite when the parent solution is depleted in
229 magnesium, whereas it concentrates in calcite, when the parent solution is enriched in
230 magnesium (Rude and Aller 1991), and as magnesium concentrations rise, so too does the
231 concentration of fluorine in calcite (Kitano and Okumura 1973). Dissolution of aragonite and
232 Mg-calcite during diagenesis releases F^- into pore waters, where it may be consumed during the
233 formation of fluorapatite or adsorbed during the reprecipitation of calcium-iron carbonates, Fe-
234 oxyhydroxides, and Mn-oxides (Rude and Aller 1991). In the case of calcite and Fe-calcite, F^-
235 has been shown to be removed from solution by: a) by adsorption onto the surface of calcite,
236 demonstrated in calcite nano particles, at low F^- concentrations (<5 ppm) (Budyanto et al., 2015)
237 and high pH (Padhi and Tokunaga 2015); and b) from the precipitation of fluorite on the surface
238 of the calcite at concentrations greater than 10 ppm (Budyanto et al., 2015) and low pH (Padhi
239 and Tokunaga 2015).

240 Carbonate cements in the Newburn H-23 well show a complex history of formation,
241 dissolution, and re-precipitation. Ankerite, calcite and Mg-calcite are the earliest diagenetic
242 carbonate minerals, which were later replaced by Fe-calcite and F-rich Fe-calcite, and finally by
243 siderite (Fig. 4). Of these minerals only Fe-calcite contains fluorine >1 wt.%, suggesting that the
244 conditions for fluorine enrichment existed under only particular diagenetic conditions that post-

245 dated the main release of bicarbonate ions associated with maturation of organic matter (Karim
246 et al. 2012), but predating high temperature corrosive brines that precipitated fibrous chlorite,
247 late siderite and sphalerite seen farther up-dip in wells on the Scotian Shelf (Pe-Piper et al.
248 2015).

249 High F^- contents of formation waters are always associated with high Cl^- contents
250 (Worden 1996). At the concentrations of Cl^- estimated from saline fluid inclusions with 20%
251 $NaCl_{eq}$. (Karim et al., 2012), concentrations of 10-20 ppm of F^- are expected in formation waters.
252 The correlation of F^- with Cl^- indicates that the principal source of both halogens to formation
253 waters is from evaporites (Worden 1996). Samples of halite from the salt canopy at the
254 Weymouth A-45 well contain fluorite inclusions (G. Pe-Piper, unpublished data). The strong
255 influence of the Argo salt on formation waters and diagenesis, with hydrocarbon charge during
256 late diagenesis (Pe-Piper et al., 2015), indicate that conditions of F^- concentration >10 ppm and
257 low pH (from organic acids) are likely to have obtained.

258

259 **Diagenetic zircon**

260 The small euhedral zircons with textural relationships suggesting a late diagenetic origin
261 (Fig. 10) may alternatively be volcanogenic, derived from Early Cretaceous volcanoes to the
262 northeast. They are morphologically comparable with the smaller zircons dated by Piper et al.
263 (2012). Zircon would have experienced less dissolution and overgrowth at temperatures ~ 100 °C
264 than the major framework minerals quartz and feldspar, thus appearing to be of later diagenetic
265 origin. The U-Pb data are consistent with either a diagenetic or detrital origin.

266 Zircon is typically thought of as being a refractory mineral which endures all the stages
267 of diagenesis with minimal effect on its composition and crystal structure. However, several
268 recent studies suggest that zircon may be more susceptible to dissolution and overgrowths than

269 previously thought. Diagenetic zircon described in the literature (Rasmussen 2005; Bojanowski
270 et al. 2012) shows varying morphologies, some of which resemble the morphologies of zircon of
271 this study. Outgrowths similar to those in Figure 11 have been shown to form as minute irregular
272 crystals attached to detrital zircon grains (Rasmussen 2005, their figs. 3 and 4). These irregular
273 crystals are typically less than 3 μm in size and are commonly in “frilly rims” that partly
274 surround detrital zircon, and can also line the surface of fragments of detrital zircon (Rasmussen
275 2005, their figs. 5, 6).

276 Detrital zircon grains from low grade metamorphic rocks have darker patches in BSE
277 images, similar to those in our Figure 11D, that represent zones of low temperature dissolution
278 and reprecipitation of metamict zircon. Such zircon alteration has been reported from rocks with
279 a maximum temperature of 300-350°C (Hay and Dempster 2009). The liberated zirconium is
280 mobilized from areas of low temperature alteration and forms outgrowths on the margins of
281 unmodified zircon crystals.

282 Analogous dissolution and reprecipitation of existing zircon grains is also reported in
283 anchimetamorphic sedimentary rocks, where it is facilitated by high concentrations of F^- ,
284 phosphate (PO_4^{3-}), and carbonate in hydrothermal fluids at temperatures as low as 270° C
285 (Bojanowski et al., 2012). Irregular outgrowths, similar to those in our Figure 11, form in
286 prehnite-pumpellyite grade shales at 250° C (Rasmussen 2005).

287 The characteristics of the fluids responsible for the mobilization of zirconium vary. High
288 concentrations of zirconium have been documented in alkaline fluids with pH values of ~10
289 (Vard and Williams-Jones 1993) and ~12 (Kraynov et al., 1969). Solubility experiments by Aja
290 et al. (1995) on zirconium bearing minerals showed that $\text{Zr}(\text{OH})_4(\text{aq})$ is the dominant form in
291 which zirconium is transported in solution over a wide variety of pH conditions. However, the

292 mobility of zirconium is promoted by the presence of ligands in solution, principally F^- and PO_4^{3-}
293 anions (Gieré 1990), which form complexes with zirconium and allow for the typically immobile
294 element to be transported in solution. F^- is particularly effective under acid conditions (Aja et al.,
295 1995), as a content of between 0 and 6 wt.% F^- in solution increases the solubility of zirconium
296 by its square (Rubin et al., 1993). Decreases in ligand activity within a solution facilitate the
297 removal of zirconium from solution, particularly during the formation of minerals which contain
298 the complexing elements (Gieré 1986, 1990). Aja et al. (1995) suggested that zirconium is
299 transported by F^- rich, calcium (Ca^{2+}) deficient fluids which precipitate fluorite and zirconium
300 bearing phases when the fluids interact either with Ca^{2+} rich fluids or calcium bearing host rocks
301 which destabilize the zirconium and F^- complexes. Clay minerals such as kaolinite and chlorite
302 can adsorb F^- onto their surfaces by exchanging hydroxyl groups (OH^-) for F^- at surface active
303 hydroxyl sites (Du et al., 2011). At low concentrations the exchange can only occur if the OH^-
304 group is protonated by H^+ from a low pH solution. However, as concentrations of F^- increase to
305 >5 ppm for kaolinite and >100 ppm for chlorite, the exchange no longer requires low pH
306 solutions.

307 In the Newburn H-23 well, several late diagenetic minerals contain F^- and PO_4^{3-} anions,
308 including apatite, fluorapatite, fluorite, and F-rich Fe-calcite. Since these anions are major
309 ligands for zirconium, precipitation of these minerals may have led to the precipitation of
310 diagenetic zircon outgrowths. Calcite is present in the majority of studied samples; it is generally
311 an early formed mineral and is easily dissolved by highly acidic fluids such as the ones required
312 to transport zirconium. Calcite grains in the Newburn H-23 well commonly show dissolution
313 voids, replacement by other minerals, and ragged grain boundaries. The dissolution and
314 replacement of these grains would have produced pore fluids rich in Ca^{2+} , and could have mixed

315 with the F^- and PO_4^{3-} rich fluids which were complexing zirconium, thereby precipitating apatite,
316 fluorapatite, fluorite, and F-rich Fe-calcite.

317 Chlorite and kaolinite are common pore filling minerals in the Newburn H-23 well. SEM
318 analysis did not detect fluorine in any grains of kaolinite, however several analyses of chlorite
319 grains showed the presence of fluorine (Fig. 9). The acidic solution carrying zirconium and its
320 ligands would have facilitated the exchange of OH^- groups and the adsorption of F^- . Such
321 surficial adsorption onto chlorite and other framework grains may have played a role in the
322 removal of F^- ligands from zirconium bearing fluids. Based on the estimate of 10–20 ppm F^- in
323 the Scotian Basin brines, the critical concentration of 100 ppm for adsorption of F^- on chlorite
324 was probably achieved only under exceptional local conditions.

325 In summary, two processes led to removal of ligands from solution and consequent
326 precipitation of zircon. (1) Formation of fluorine and phosphorus bearing minerals such as
327 apatite, fluorapatite, fluorite, and F-Fe-calcite via the dissolution of calcite, and interaction of the
328 zirconium bearing fluids with liberated Ca^{2+} ; and (2) the surficial adsorption of F^- onto chlorite
329 and framework grains.

330 The high temperature diagenetic mineral sphalerite is present in all studied stratigraphic
331 levels in the Newburn H-23 well. A salinity of $\sim 17\%$ $NaCl_{eq}$ is required for major transport of
332 zinc in chloride complexes (Hanor, 1996), although some brines with $>10\%$ salinity may
333 transport zinc (Giordano, 2002). Crystallization of sphalerite generally occurs at temperatures of
334 140° – $200^\circ C$ (Samson and Russell, 1987). This is a little lower than temperatures in the literature
335 for diagenetic zircons ($\sim 270^\circ C$) and outgrowths ($\sim 250^\circ C$) (Rasmussen, 2004; Bojanowski et al.
336 2012).

337 **Thermal history of the Scotian Basin and its relationship to diagenetic zircon**

338 A widespread thermal event in the Scotian Basin during the Aptian-Albian is recorded by
339 volcanism in the Orpheus graben and enhanced heat flow in terrestrial basins (Bowman et al.
340 2012), high homogenization temperature of primary fluid inclusions in quartz overgrowths and
341 carbonate cements (Fig. 12), and by strongly negative $\delta^{13}\text{C}$ in carbonate cements of that age
342 (Karim et al. 2012). This event increased the temperature of circulating brines, as shown in
343 calculated trapping temperatures in quartz overgrowths that are as high as 228°C and in
344 carbonate cements as high as 189°C in the Lower Missisauga Formation in the Thebaud well
345 (Karim et al. 2012). This thermal event was likely the result of a regional process in the mantle,
346 probably related to the rifting of Iberia and the Grand Banks (Pe-Piper et al. 2007). This event
347 increased the regional geothermal gradient to 55°C/km (Karim et al. 2012). The presence in the
348 Glenelg field, up-dip from Newburn H-23, of diagenetic sphalerite post-dating carbonate
349 cements, was correlated with Albian-Cenomanian movement on the Balvenie salt Roho system
350 (Pe-Piper et al. 2015).

351 Flow of hot brines was potentially sourced from compaction of sediment in the deep
352 basin and migration along detachment faults, down-to-basin listric faults, and permeable
353 sandstones (Pe-Piper et al. 2015). Seaward of Newburn H-23, the original Triassic rift basin with
354 autochthonous salt lies about 3.5 s below the Albian K095 seismic marker (Fig. 1B: Deptuck et
355 al. 2009), which using an average seismic velocity of 4.0 km/s (Shimeld 2004) gives a burial
356 depth of 7 km. Using a geothermal gradient of 40°C/km based solely on lithospheric cooling and
357 a sea floor temperature of 30°C, as justified by Karim et al. (2012), the temperature of the
358 autochthonous salt would conservatively be 310°C. Using an elevated geothermal gradient of
359 55°C/km as suggested by Wierzbicki et al. (2006) and Karim et al. (2012), the autochthonous

360 salt and underlying syn-rift sediments and continental basement rocks would reach temperatures
361 of >400°C, resulting in low-grade metamorphism. At these temperatures, pre-existing zircons
362 would suffer low temperature dissolution as described by Hay and Dempster (2009).

363 Normally at such low-grade metamorphic temperatures, zircon alteration is pervasive in
364 metamict zircon and dissolution-reprecipitation processes occur locally, producing outgrowths
365 on the margins of original zircon crystals (Hay and Dempster 2009). However, in the presence of
366 high F⁻ ion concentrations from interbedded halite, and under somewhat acid conditions from the
367 maturation of organic matter, zirconium dissolved from zircons will complex with F⁻ and is
368 capable of long-distance transport in migrating basinal brines (Fig. 12). It produced outgrowths
369 on pre-existing zircons in sandstone at Newburn H-23 (Fig. 11) and may have precipitated
370 neoformed diagenetic zircon crystals (Fig. 10A, E). The formation of outgrowths on zircon
371 grains in metamorphic environments have been suggested to form as the result of a decrease in
372 temperature during retrograde metamorphism (Hay and Dempster 2009). The outgrowths
373 metamorphic rocks are commonly found to be interfingered with muscovite and chlorite,
374 suggesting that they are contemporaneous with or younger than these metamorphic minerals. The
375 formation of similar diagenetic outgrowths of zircon in the Newburn H-23 well may also be an
376 indicator of cooling following a period of elevated geothermal gradient in the Aptian–Albian,
377 during which zirconium was readily released from zircon. The unusual occurrence of diagenetic
378 zircon, at least as outgrowths, in the Newburn H-23 well is the result of two geological
379 conditions: the high heat flow after deep burial of syn-rift clastic sediments and salt, and the
380 presence of halite as a source of F⁻ ions.

381

IMPLICATIONS

382

383

384

385

386

387

388

389

390

391

This study has shown that hot brines with F⁻ contents of >10 ppm, derived from deep burial of thick halite successions, can be recognised from high F content of diagenetic ferroan calcite. Such brines are also able to complex with zirconium from dissolved metamict detrital zircon under low grade metamorphic conditions of deep burial to produce diagenetic zircon outgrowths and probably neoformed zircon crystals. Zircon diagenesis is favored by elevated heat flow producing a geothermal gradient >50°C/km, in order to achieve metamorphic temperatures at which zirconium is readily released from zircon. Suitable geological conditions are found where a subsiding rift basin with early evaporites is affected by a subsequent phase of volcanism due to new rifting or subduction.

392

CONCLUSIONS

393

394

395

396

397

398

The Newburn H-23 well is the closest well with samples for diagenetic studies to the deep-water depocenter of the Scotian Basin. It has late-diagenetic fluorine-rich ferroan calcite cement, with <2.5 wt.% fluorine, mostly at a <1 µm scale presumably by adsorption, but also locally as small fluorite crystals. Fluorine is also apparently adsorbed on the surfaces of some framework minerals and in chlorite. The abundance of fluorine is related to the highly saline formation brines derived from the Argo salt Formation.

399

400

401

402

The unusual occurrence of outgrowths on zircons, and the possible presence of neoformed diagenetic zircon, is the result of zirconium mobility in the presence of >10 ppm concentration of F⁻ in formation brines. It also required high temperatures (likely ~400°C) in syn-rift clastic sediment interbedded with the Argo salt Formation, resulting from regional high

403 heat flow in the Aptian–Albian, some 60 Ma after initial sea-floor spreading in the basin, that led
404 to low-grade metamorphic dissolution of patches of metamict zircon.

405

406

ACKNOWLEDGEMENTS

407 We thank the Canada Nova Scotia Offshore Petroleum Board (CNSOPB) for providing
408 all the samples, and Andrew MacRae for his help in securing the sidewall core samples. We also
409 thank Xiang Yang and Randolph Corney for their advice with the SEM and polished thin
410 sections. Special thanks to David Piper for critically reviewing this paper. The funding for this
411 project was provided by Encana (administrated by the Offshore Energy Research Association,
412 OERA), and the Natural Sciences and Engineering Research Council of Canada (NSERC).

413

REFERENCES CITED

- 414 Aja, S.U., Wood, S.A., and Williams-Jones, A.E. (1995) The aqueous geochemistry of Zr and
415 the solubility of some Zr-bearing minerals. *Applied Geochemistry*, 10, 603-620.
- 416 Albertz, M., Beaumont, C., Shimeld, J., Ings, S.J., and Gradmann, S. (2010) An investigation of
417 salt tectonics structural styles in the Scotian Basin, offshore Atlantic Canada: 1.
418 Comparison of observations with geometrically simple numerical models. *Tectonics*, 29,
419 doi:10.1029/2009TC002539.
- 420 Bojanowski, M.J., Bagin´ski, B., Clarkson, E., Macdonald, R., and Marynowski, L. (2012) Low-
421 temperature zircon growth related to hydrothermal alteration of siderite concretions in
422 Mississippian shales, Scotland. *Contributions to Mineralogy and Petrology*, 164, 245-259.
- 423 Bowman, S.J., Pe-Piper, G., Piper, D.J.W., Fensome, R.A., and King, E. L. (2012) Early
424 Cretaceous volcanism in the Scotian Basin. *Canadian Journal of Earth Sciences*, 49(12),
425 523-1539.

- 426 Budyanto, S., Kuo, Y., and Liu, J.C. (2015) Adsorption and precipitation of fluoride on calcite
427 nanoparticles: A spectroscopic study. *Separation and Purification Technology*, 150,
428 325-331.
- 429 Chevron Corporation et al. (2002) Well History Report for Newburn H-23 at Exploration
430 Licence Area 2359 off the Scotian Shelf, Offshore, Nova Scotia. Available from Canada-
431 Nova Scotia Offshore Petroleum Board.
- 432 Cummings, D.I., and Arnott., R.W.C. (2005) Growth-faulted shelf-margin deltas: a new (but old)
433 play type, offshore Nova Scotia. *Bulletin of Canadian Petroleum Geology*, 53, 211-236.
- 434 Deptuck, M. E., Kendall, K., and Smith, B. (2009) Complex deepwater fold belts in the SW
435 Sable Subbasin, offshore Nova Scotia. Canadian Society of Petroleum
436 Geologists/Canadian Society of Exploration Geophysicists/Canadian Well Logging Society
437 Convention, p. 4, Society of Exploration Geophysicists/Canadian Well Logging Society,
438 Alberta.
- 439 Du, J., Wu, D., Xiao, H., and Li, P. (2011) Adsorption of fluoride on clay minerals and their
440 mechanisms using X-ray photoelectron spectroscopy. *Frontiers of Environmental Science*
441 *& Engineering in China*, 2, 212-226
- 442 Gieré, R. (1986) Zirconolite, allanite and hoegbomite in a marble skarn from the Bergell contact
443 aureole: implications for mobility of Ti, Zr and REE. *Contributions to Mineralogy and*
444 *Petrology*, 93, 459-470
- 445 Gieré, R. (1990) Hydrothermal Mobility of Ti, Zr and REE: Examples from the Bergell and
446 Adamello Contact Aureoles (Italy). *Terra nova*, 2, 60-67.

- 447 Giordano, T.H. (2002) Transport of Pb and Zn by carboxylate complexes in basinal ore fluids
448 and related petroleum-field brines at 100°C: The influence of pH and oxygen fugacity.
449 Geochemical Transactions, 3(1), 56-72.
- 450 Gould, K., Pe-Piper, G., and Piper, D.J.W. (2010) Relationship of diagenetic chlorite rims to
451 depositional facies in Lower Cretaceous reservoir sandstones of the Scotian Basin.
452 Sedimentology, 57, 587-610
- 453 Hanor, J.S. (1996) Variations in chloride as a driving force in siliciclastic diagenesis. In L. J.,
454 Crossey, R., Loucks, M.W., Totten, and P.A., Scholle, Eds., Siliciclastic diagenesis and
455 fluid flow: Concepts and applications, 55, 4-12 p., SEPM Special Publication, Oklahoma.
- 456 Hay, D.C., and Dempster, T.J. (2009) Zircon Behaviour during Low-temperature
457 Metamorphism. Journal of Petrology, 50, 571-589.
- 458 Holser, W.T., Clement, G.P., Jansa, L. and Wade, J.A. (1988) Evaporite deposits of the North
459 Atlantic Rift. In W., Manspeizer, Ed., Triassic-Jurassic Rifting: Continental Breakup and
460 the Origin of the Atlantic Ocean and Passive Margins, 525-556 p., Elsevier, Amsterdam.
- 461 Karim, A., Pe-Piper, G., and Piper, D.J.W. (2010) Controls on diagenesis of Lower Cretaceous
462 reservoir sandstones in the western Sable Subbasin, offshore Nova Scotia. Sedimentary
463 Geology, 224, 65-83.
- 464 Karim, A., Hanley, J.J., Pe-Piper, G., and Piper, D.J.W. (2012) Paleohydrogeological and
465 thermal events recorded by fluid inclusions and stable isotopes of diagenetic minerals in
466 Lower Cretaceous sandstones, offshore Nova Scotia, Canada. AAPG Bulletin, 96(6),
467 1147-1169.
- 468 Kendell, K.L. (2012) Variations in salt expulsion style within the Sable Canopy Complex,
469 central Scotian margin. Canadian Journal of Earth Sciences, 49, 1504-1522.

- 470 Kidston, A.G., Smith, B., Brown, D.E., Makrides, C. and Altheim, B. (2007) Nova Scotia Deep
471 Water Offshore Post-Drill Analysis - 1982-2004, 181 p. Canada-Nova Scotia Offshore
472 Petroleum Board, Nova Scotia.
- 473 Kitano, Y., and Okumura, M. (1973) Coprecipitation of fluoride with calcium carbonate.
474 *Geochemical Journal*, 7, 37-49.
- 475 Kraynov, S.R., Mer'kov, A.N., Petrova, N.G., Baturinskaya, I.V., and Zharikova V.M. (1969)
476 Highly alkaline (pH 12) fluosilicate waters in the deeper zones of the Lovozero massif.
477 *Geochemistry International USSR*, 6(4), 635-640.
- 478 Li, G., Ravenhurst, C., and Zentilli, M. (1995) Implications of apatite fission track analysis for
479 the thermal history of the Scotian Basin, offshore Nova Scotia, Canada. *Bulletin of*
480 *Canadian Petroleum Geology*, 43, 127-144
- 481 OETR (Offshore Energy Technical Research), 2011, Atlas: Play Fairway Analysis, Offshore
482 Nova Scotia, Canada. (<http://www.webcitation.org/6kTGN6l6m>, accessed Sept. 12, 2016).
- 483 Padhi, S., and Tokunaga, T. (2015) Surface complexation modeling of fluoride sorption onto
484 calcite. *Journal of Environmental Chemical Engineering*, 3, 1892-1900.
- 485 Pe-Piper, G., Piper, D.J.W., Jansa, L.F., and de Jonge, A. (2007) Early Cretaceous opening of the
486 North Atlantic Ocean: Implications of the petrology and tectonic setting of the Fogo
487 Seamounts off the SW Grand Banks, Newfoundland. *Geological Society of America*
488 *Bulletin*, 119, 712-724
- 489 Pe-Piper, G., Piper, D.J.W., Zhang, Y., and Chavez, I. (2015) Diagenetic barite and sphalerite in
490 middle Mesozoic sandstones, Scotian Basin, as tracers for basin hydrology. *Bulletin of the*
491 *American Association of Petroleum Geologists*, 99, 1281-1313.

- 492 Piper, D.J.W., Pe-Piper, G., Tubrett, M., Triantafyllidis, S., and Strathdee, G. (2012) Detrital
493 zircon geochronology and polycyclic sediment sources, Upper Jurassic-Lower Cretaceous
494 of the Scotian Basin, southeastern Canada. *Canadian Journal of Earth Sciences*, 49, 1540-
495 1557.
- 496 Rasmussen, B. (2005) Zircon growth in very low grade metasedimentary rocks: evidence for
497 zirconium mobility at ~250°C. *Contributions to Mineral Petrology*, 150, 146-155.
- 498 Rubin, J.N., Henry, C.D., and Price, J.G. (1993) The mobility of zirconium and other "immobile"
499 elements during hydrothermal alteration. *Chemical Geology*, 110, 29-47.
- 500 Rude, P.D, and Aller, R.C. (1991) Fluorine mobility during early diagenesis of carbonate
501 sediment: An indicator of mineral transformations. *Geochimica et Cosmochimica Acta*,
502 55, 2491-2509.
- 503 Samson, I.M., and Russell, M.J. (1987) Genesis of the Silvermines zinc-lead-barite deposit,
504 Ireland: Fluid inclusion and stable isotope evidence. *Economic Geology*, 82(2), 371-394
- 505 Shimeld, J. (2004) A comparison of salt tectonic subprovinces beneath the Scotian Slope and
506 Laurentian Fan. In P. Post, D. Olson, K. Lyons, S. Palmes, P. Harrison, and N. Rosen,
507 Eds., *Salt-sediment interactions and hydrocarbon prospectivity: Concepts, applications,*
508 *and case studies for the 21st century*, 24th Annual Gulf Coast Section SEPM Foundation
509 Bob F. Perkins Research Conference Proceedings, p. 502-532, SEPM Foundation, Texas,
510 doi:10.5724/gcs.04.24.0502.
- 511 Vard, E., and Williams-Jones, A.E. (1993) A fluid inclusion study of vug minerals in dawsonite-
512 altered phonolite sills, Montreal, Quebec: implications for HFSE mobility. *Contributions to*
513 *Mineralogy and Petrology*, 113, 410–423

- 514 Wade, J.A., and MacLean, B.C. (1990) Aspects of the geology of the Scotian Basin from recent
515 seismic and well data. In M.J. Keen and G.L. Williams Eds., *Geology of the Continental*
516 *Margin of Eastern Canada*, p. 167–238, Geological Survey of Canada, Ottawa, Canada.
- 517 Wade, J.A., Williams, G.L., and MacLean, B.C. (1995) Mesozoic and Cenozoic stratigraphy,
518 eastern Scotian Shelf: new interpretations. *Canadian Journal of Earth Sciences*, 32(9),
519 1462-1473.
- 520 Weston, J.F., MacRae, R.A., Ascoli, P., Cooper, M.K.E., Fensom, R.A., Shaw, D., and Williams,
521 G.L. (2012) A revised biostratigraphic and well-log sequencestratigraphic framework for
522 the Scotian Margin, offshore eastern Canada. *Canadian Journal of Earth Sciences*, 49,
523 1417-1462.
- 524 Wierzbicki, R., Dravis, J., Al-Aasm, I., and Harland, N. (2006) Burial dolomitization and
525 dissolution of upper Jurassic Abenaki platform carbonates, Deep Panuke reservoir, Nova
526 Scotia, Canada. *American Association of Petroleum Geology*, 90, 1843-1861
- 527 Williamson, M.A. (1995) Overpressures and hydrocarbon generation in the Sable Sub-basin,
528 offshore Nova Scotia. *Basin Research*, 7, 21-34.
- 529 Worden, R.H. (1996) Controls on halogen concentrations in sedimentary formation waters.
530 *Mineralogical Magazine*, 60, 259-274.
- 531 Zhang, Y., Pe-Piper, G., and Piper, D.J.W. (2014) Sediment geochemistry as a provenance
532 indicator: unravelling the cryptic signatures of polycyclic sources, climate change,
533 tectonism and volcanism. *Sedimentology*, 61(2), 383-410.

534
535

536

FIGURE CAPTIONS

537 **Fig. 1: A:** Isopach map of the Scotian Basin showing location of Newburn H-23 well and
538 inferred paleorivers and volcanic centers in the Early Cretaceous. Base map modified from Wade
539 and MacLean (1990), volcanic centers from Bowman et al. (2012), and paleorivers and major
540 faults from Zhang et al. (2014). **B:** Cross section of part of the Scotian Basin showing geological
541 setting of the Newburn H-23 well. Stratigraphic interpretation from Deptuck et al. (2009) based
542 on 3-D seismic data.

543

544 **Fig. 2:** Stratigraphic column of the Mesozoic rocks of the Scotian basin. Modified from Weston
545 et al. (2012).

546

547 **Fig. 3:** Stratigraphic column for the Newburn H-23 well from the top of the targeted “turbidite”
548 interval showing litho- and biostratigraphy, lithology (from cuttings descriptions and wireline
549 logs), paleo-water-depth estimates from microfossil assemblages, gamma ray log, sidewall core
550 sample locations, and presence of key minerals. (Data from Chevron et al. 2002; Kidston et al.
551 2007; OETR 2011; Weston et al. 2012). brt = barite; F-Fe cal = fluorine-rich ferroan calcite; sp =
552 sphalerite; zrn og = zircon outgrowths.

553

554 **Fig. 4:** Representative BSE images of textures of Fe-calcite and other carbonates from the
555 Newburn H-23 well. Framework quartz grains appear dark. **A:** Fe-calcite engulfs albite, K-
556 feldspar, and quartz, perhaps in an original feldspathic lithic clast, and is partly replaced by
557 siderite [4353.5 m]. **B:** Calcite and Mg-calcite with microporosity are replaced by Fe-calcite.
558 Siderite fills a dissolution void in Fe-calcite [5213.5 m]. **C:** Ankerite engulfs albite, probably

559 from an original feldspar framework grain. Fe-calcite surrounds and replaces ankerite and
560 engulfs quartz overgrowths (position a) [5213.5 m]. **D:** Fibrous chlorite cuts F-rich Fe-calcite. F-
561 rich Fe-calcite engulfs quartz overgrowths (position a) [5403.6 m]. **E:** F-rich Fe-calcite engulfs
562 quartz overgrowths (position a). Chlorite cuts F-rich Fe-calcite and engulfs silt-sized quartz
563 [5403.6 m]. **F:** Calcite and F-rich Fe-calcite have dissolution voids filled by chlorite. Calcite has
564 been partly replaced by F-rich Fe-calcite [5407 m]. The contact between calcite and F-rich Fe-
565 calcite is marked by the dashed line.

566

567 **Fig. 5:** Bi-plots of calcite analyses using EMP data showing **A:** chemical definition of Calcite,
568 Fe-calcite and Low Mg-calcite; **B:** variation of F with Mg; **C:** variation of F with Fe.

569

570 **Fig. 6:** Ternary diagram of calcite EMP data from the Newburn H-23 well. **A:** Analyses plotted
571 on a fluorine, iron, and magnesium ternary diagram in element wt.%. **B:** Analyses plotted on a
572 CaCO₃, FeCO₃, and MgCO₃ ternary diagram in mole%.

573

574 **Fig. 7:** Raman spectra analyses (RSA) of F-rich Fe-calcite [5403.6 m]. Compare with reference
575 spectral lines for calcite (dashed grey lines) and fluorite (dashed black lines). **A-C:** Backscattered
576 electron images showing location of spots used for RSA analyses (1) to (7). Dots indicate
577 locations of EMP analyses (green= F-Cal; blue = F-Fe-Cal; magenta= Chl); dark minerals are
578 various calcites, bright minerals are mostly chlorite.

579

580 **Fig. 8:** BSE images from sample 5408.5 m showing a lithic clast which has been affected by late
581 cementation of F-calcite and chlorite. The location of the elemental mapping of Fig. 9 is shown.

582 In image (A), a = euhedral face of quartz overgrowth; b = Fe-calcite postdates quartz
583 overgrowth; c = secondary dissolution along quartz grain boundaries. (B) Detail of lithic clast,
584 showing porosity and platy and fibrous habits of chlorite. (C) Detail of Fe-calcite showing sparry
585 habit and porosity.

586

587 **Fig. 9:** BSE image **A:** and quantitative element mapping images **B-I:** from SEM-EDS analysis of
588 sample 5408.5 m showing the distributions of F, CaO, SiO₂, FeO, Al₂O₃, TiO₂, K₂O and Na₂O.
589 See location in Fig. 8. The color bar in the elemental maps is scaled to the quantitative EDS
590 analysis (wt.%). The intergranular boundaries are marked by solid white line.

591

592 **Fig. 10:** Representative BSE images of textural relationship of zircon to other minerals. **A:**
593 Sample 4313.5m. Zircon with sharp crystal outlines against silicate mineral and a dissolution
594 void. Trachytic lithic clast (position a). **B:** Sample 5213.5m. Zircon appears to cut framework
595 grains and Fe-calcite. **C:** Sample 5403.6m. Zircon with straight crystal outlines towards chlorite
596 (position a). **D:** Sample 5403.6m. Euhedral faces of zircon in contact with quartz and probably
597 engulfs chlorite (position a) and with euhedral crystal outlines towards both. **E:** Sample
598 5408.5m. Zircon fills pore and engulfs quartz. **F:** Sample 5961.7m. Zircon with straight crystal
599 outlines in contact with quartz and pore. **G:** Sample 5961.7m. Zircon cuts chlorite and is
600 euhedral against porosity. **H:** Sample 5961.7m. Zircon fills pore and engulfs quartz. **I:** Sample
601 5962m. Zircon and drilling mud (DM) fill porosity.

602

603 **Fig. 11:** High magnification BSE images of zircon grains. **A:** Sample 4313.5m. Zircon grain
604 showing a dark rim which is probably an outgrowth of diagenetic zircon. **B:** Sample 5403.6m.

605 Zircon grain showing outgrowths (arrows), some of which are in contact with quartz (dashed
606 line). **C:** Sample 5961.7m. Zircon grain showing abundant outgrowths (arrows). **D:** Sample
607 5961.7m. Zircon grain with abundant dissolution voids and dark patches which correspond to
608 areas with dissolution voids.

609

610 **Fig. 12.** Summary transect from Newburn H-23 to the Glenelg and Thebaud fields, showing
611 inferred thermal evolution and flow of formation waters. Measured average homogenization
612 temperatures for fluid inclusions from Karim et al. (2012): calculated entrapment temperatures
613 taking into account confining pressure tend to be tens of degrees higher. Albian geothermal
614 gradient of 40°C/km based on assumption of simple lithospheric cooling after Triassic rifting;
615 55°C/km estimated by Karim et al. (2012) from fluid inclusion studies and data of Bowman et al.
616 (2012).

617

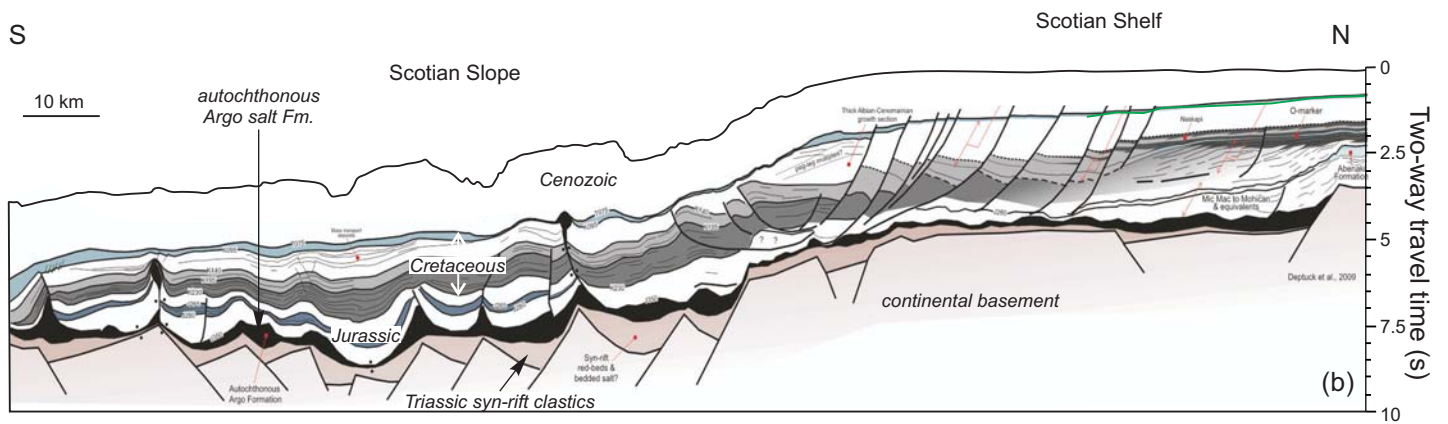
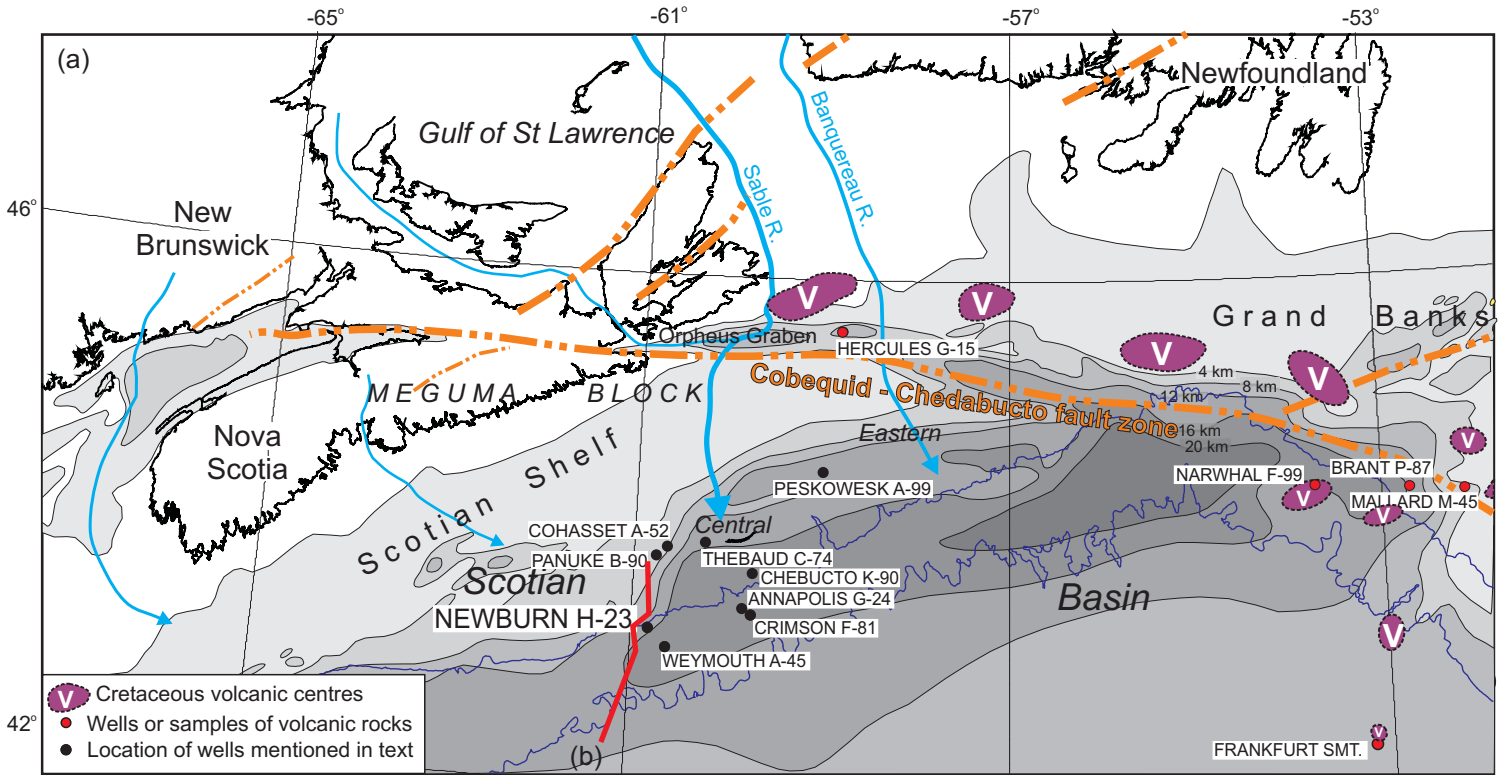


Figure 1

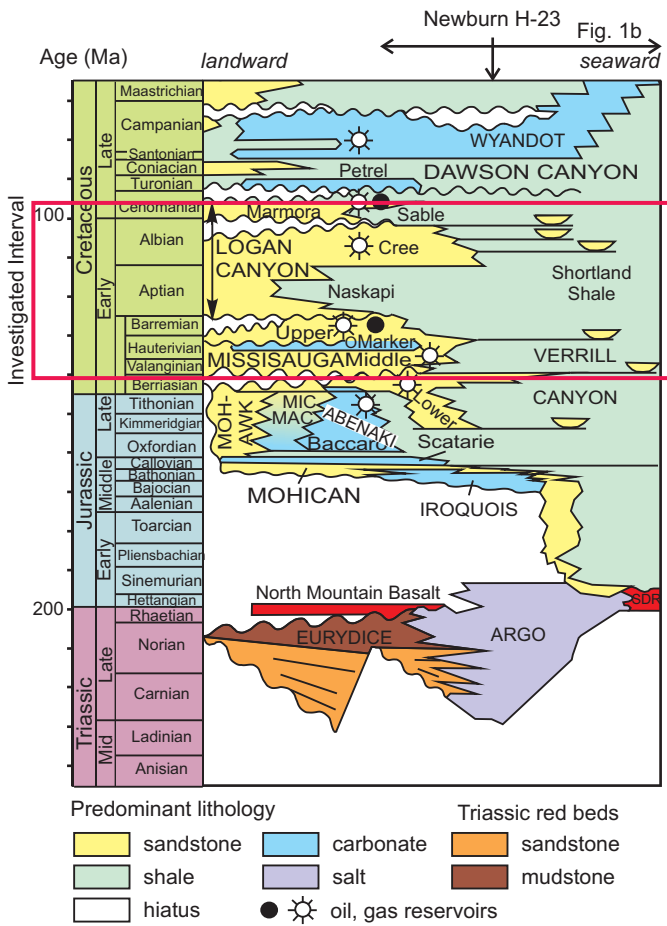


Figure 2

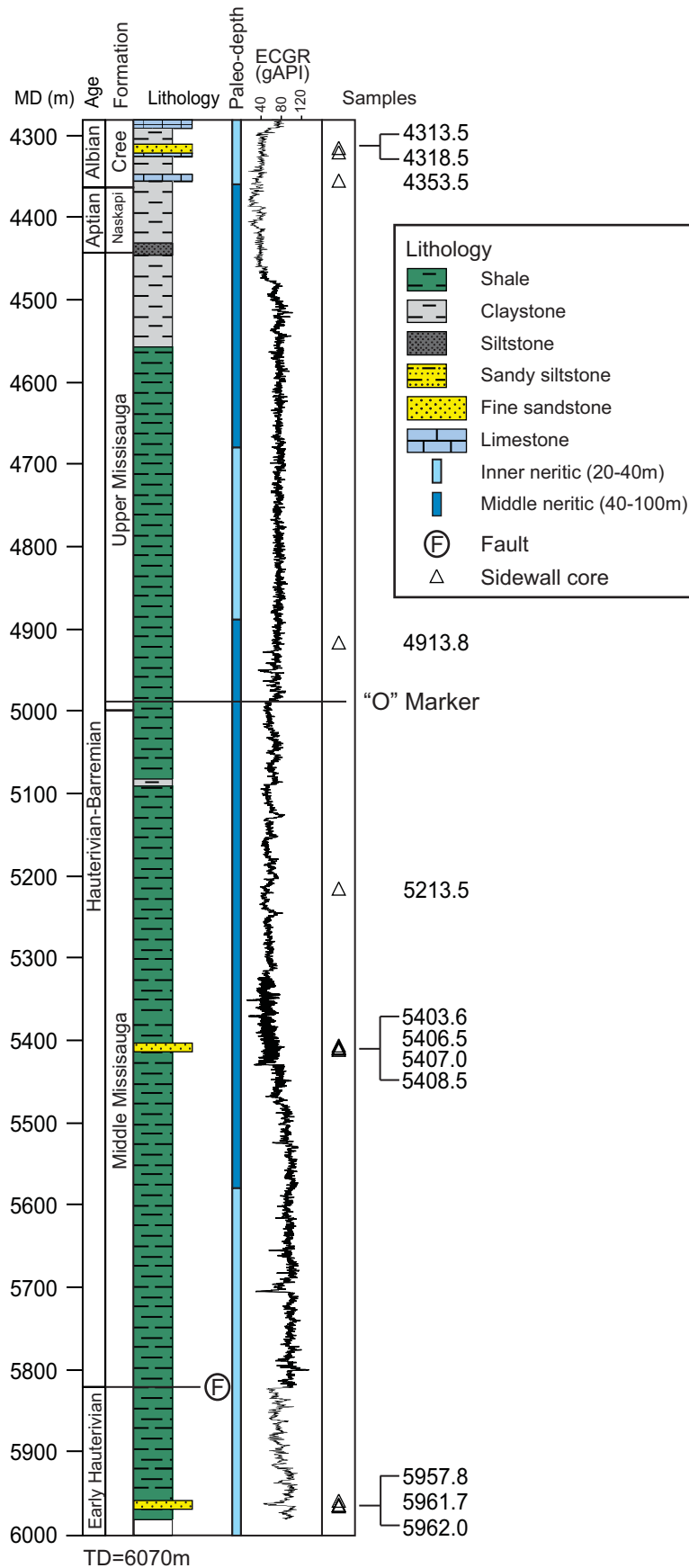


Figure 3

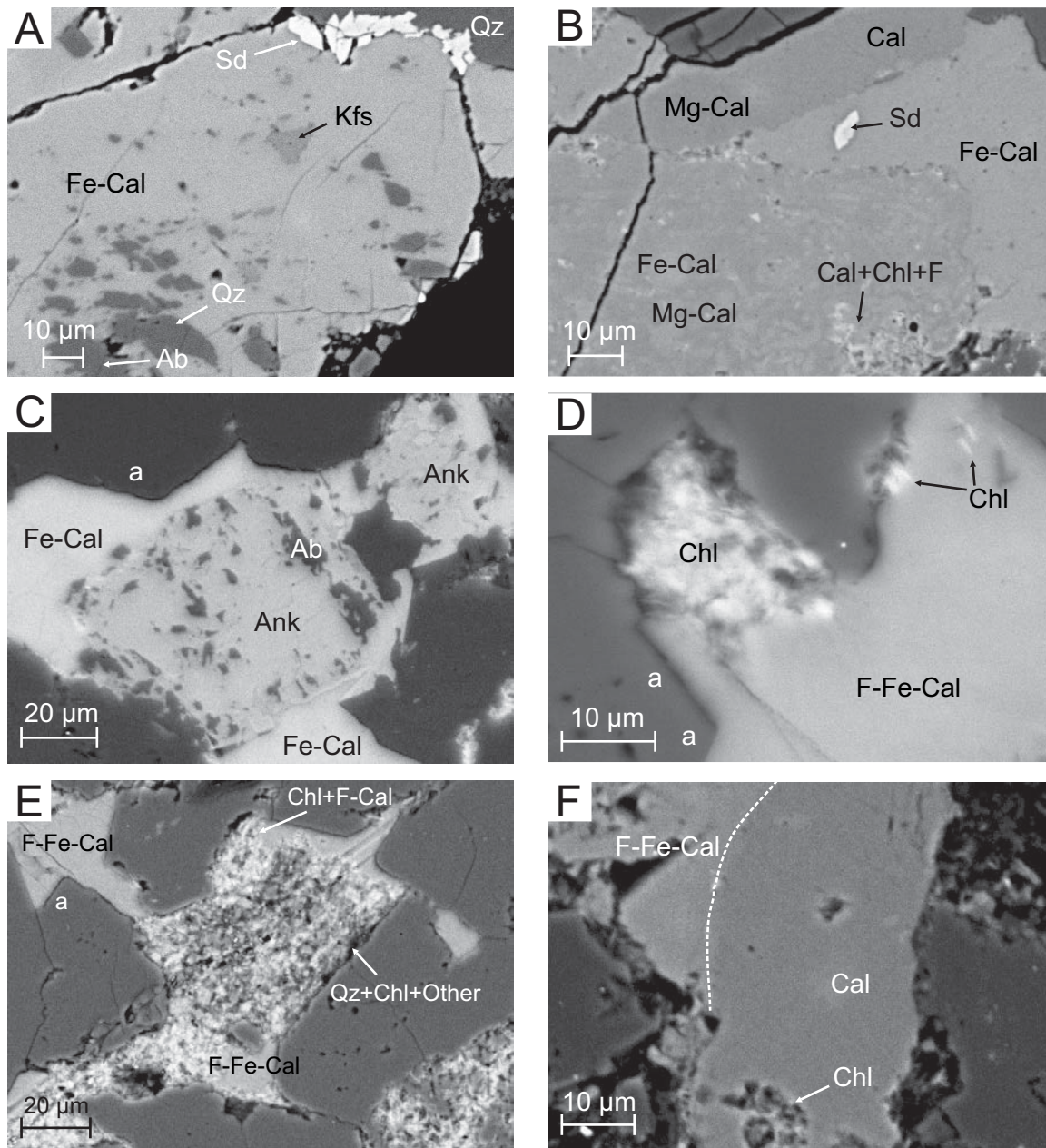


Figure 4

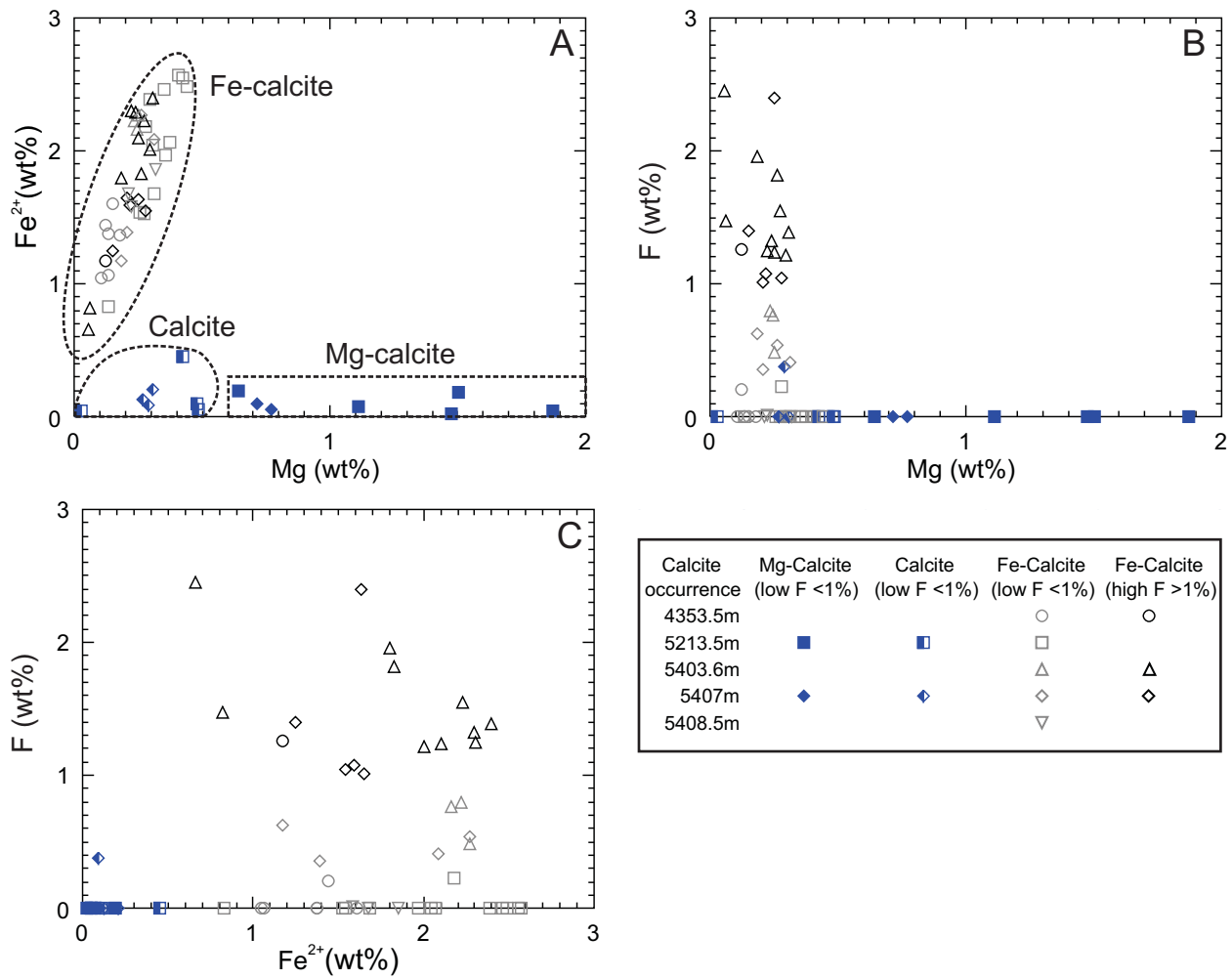
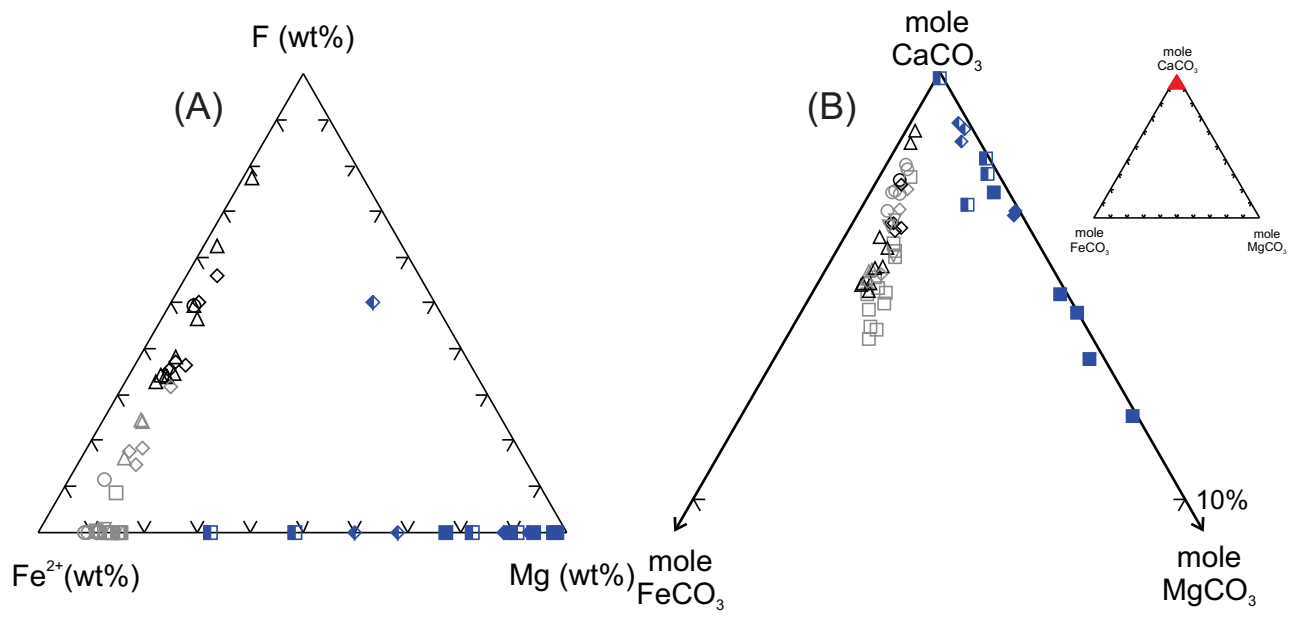


Figure 5



Calcite occurrence	Mg-Calcite (low F <1%)	Calcite (low F <1%)	Fe-Calcite (low F <1%)	Fe-Calcite (high F >1%)
4353.5m			○	○
5213.5m	■	■	□	
5403.6m			△	△
5407m	◆	◆	◇	◇
5408.5m			▽	

Figure 6

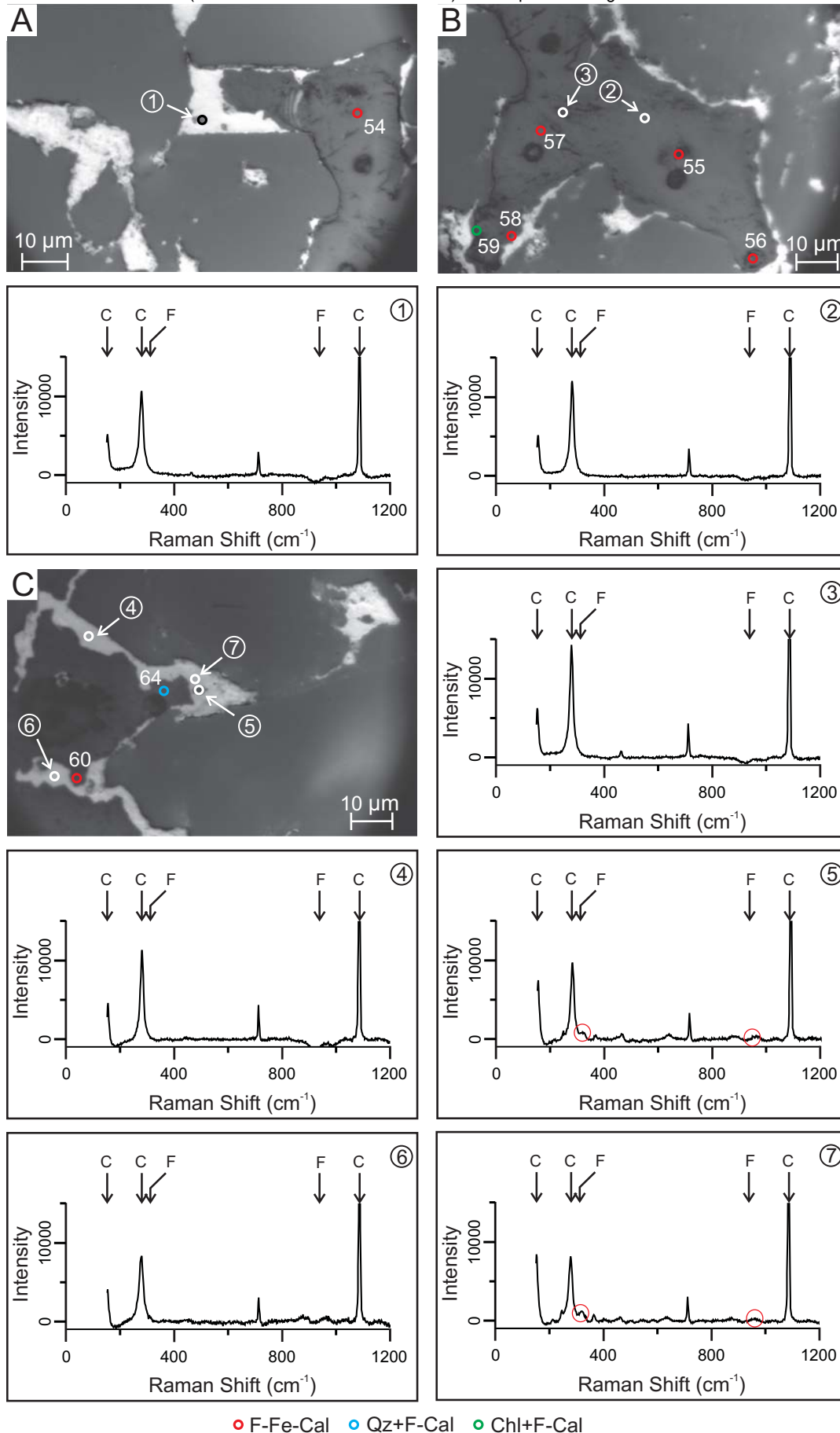


Figure 7

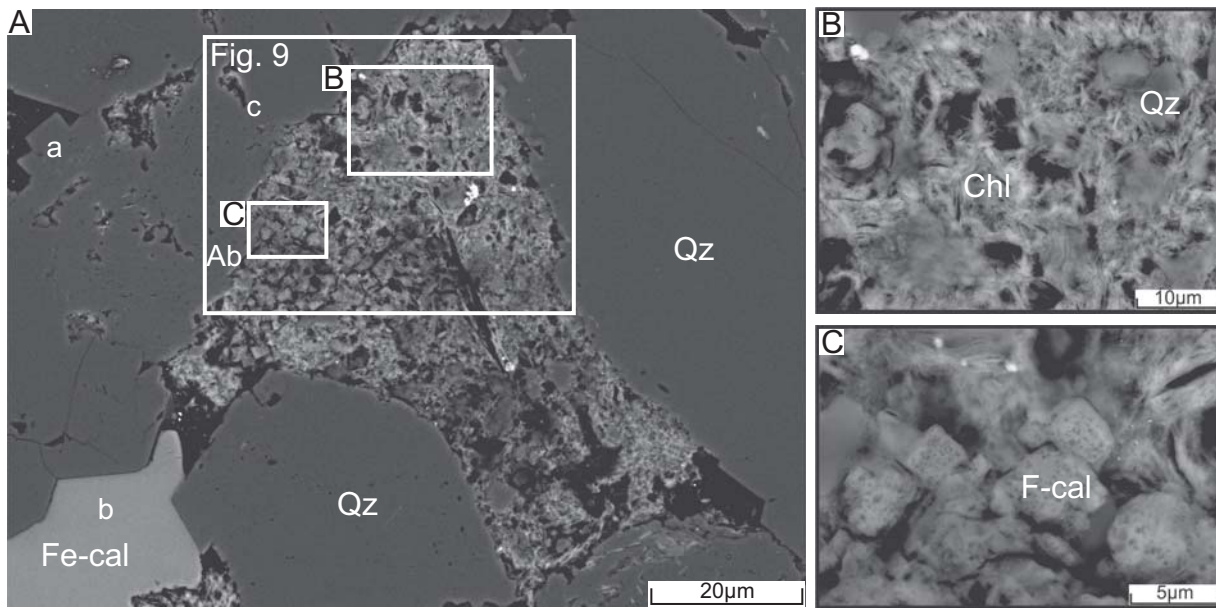


Figure 8

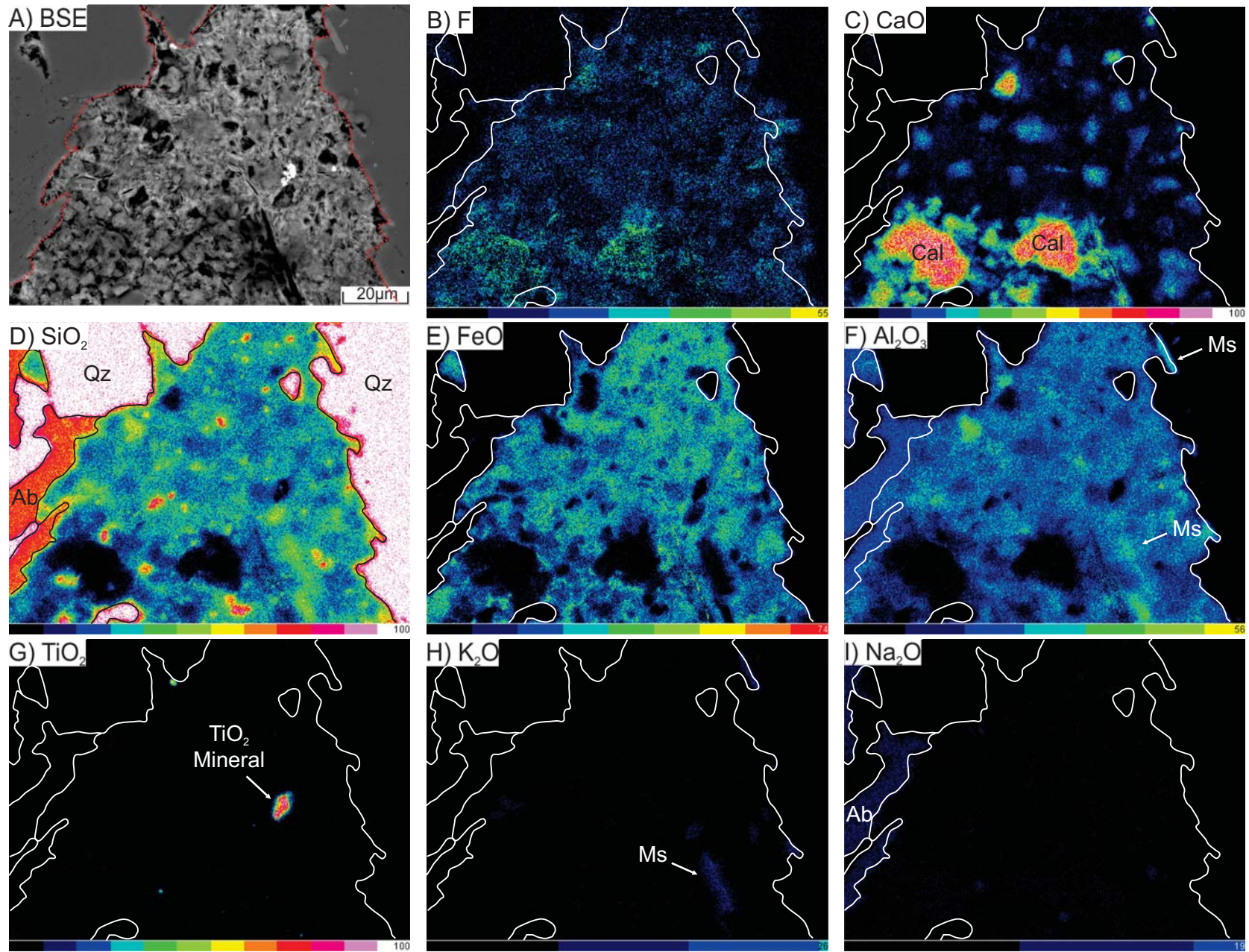


Figure 9

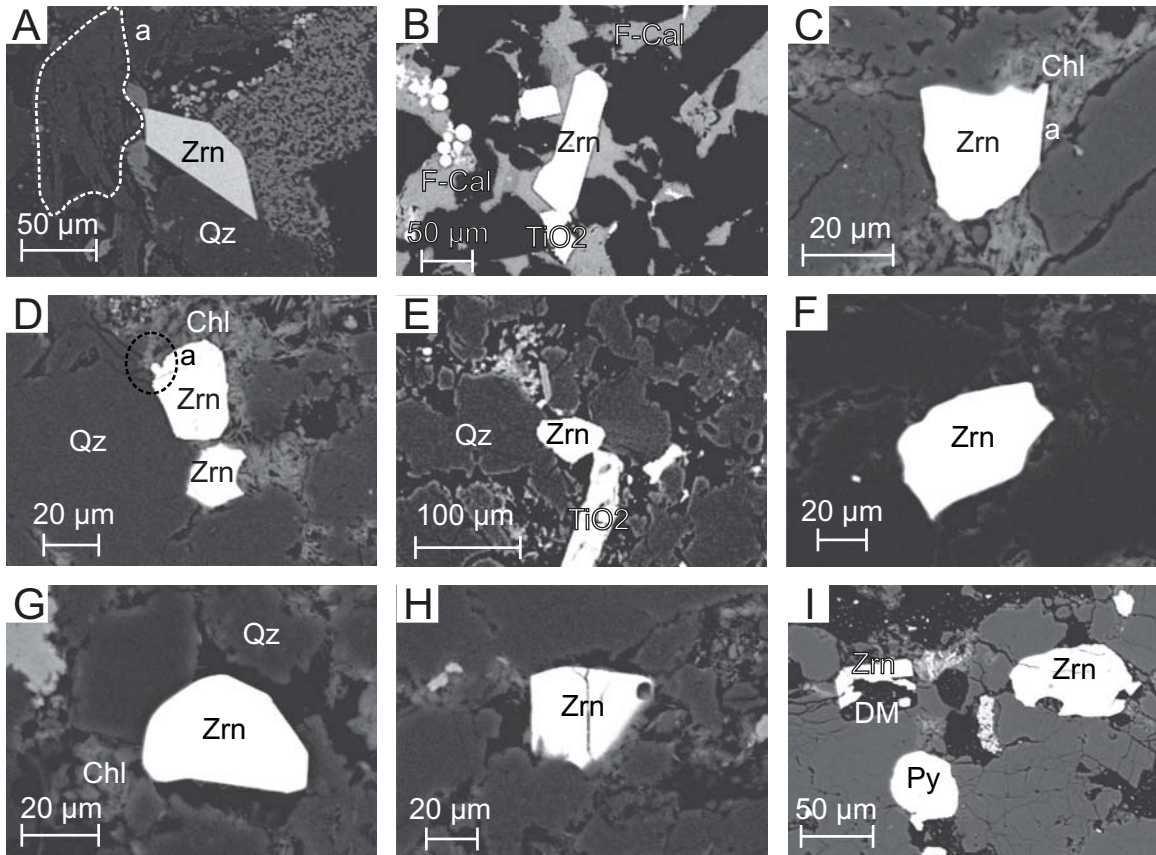


Figure 10

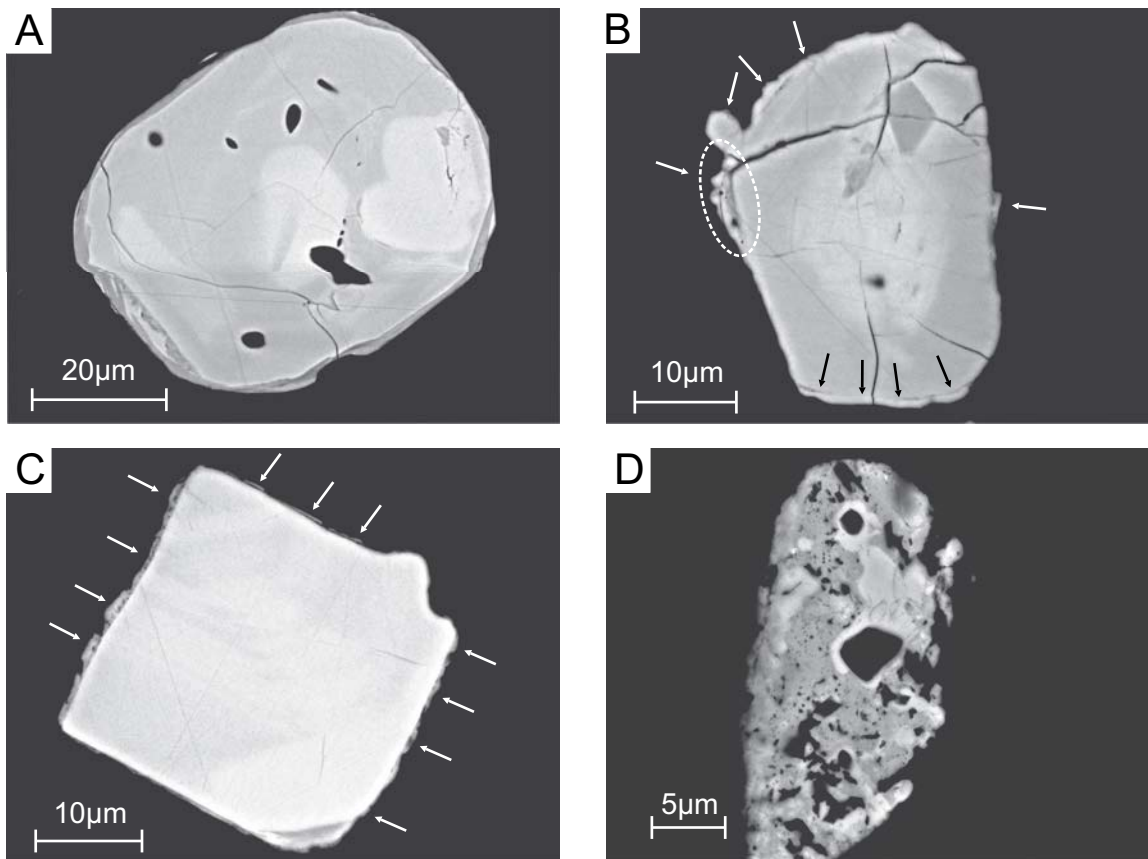


Figure 11

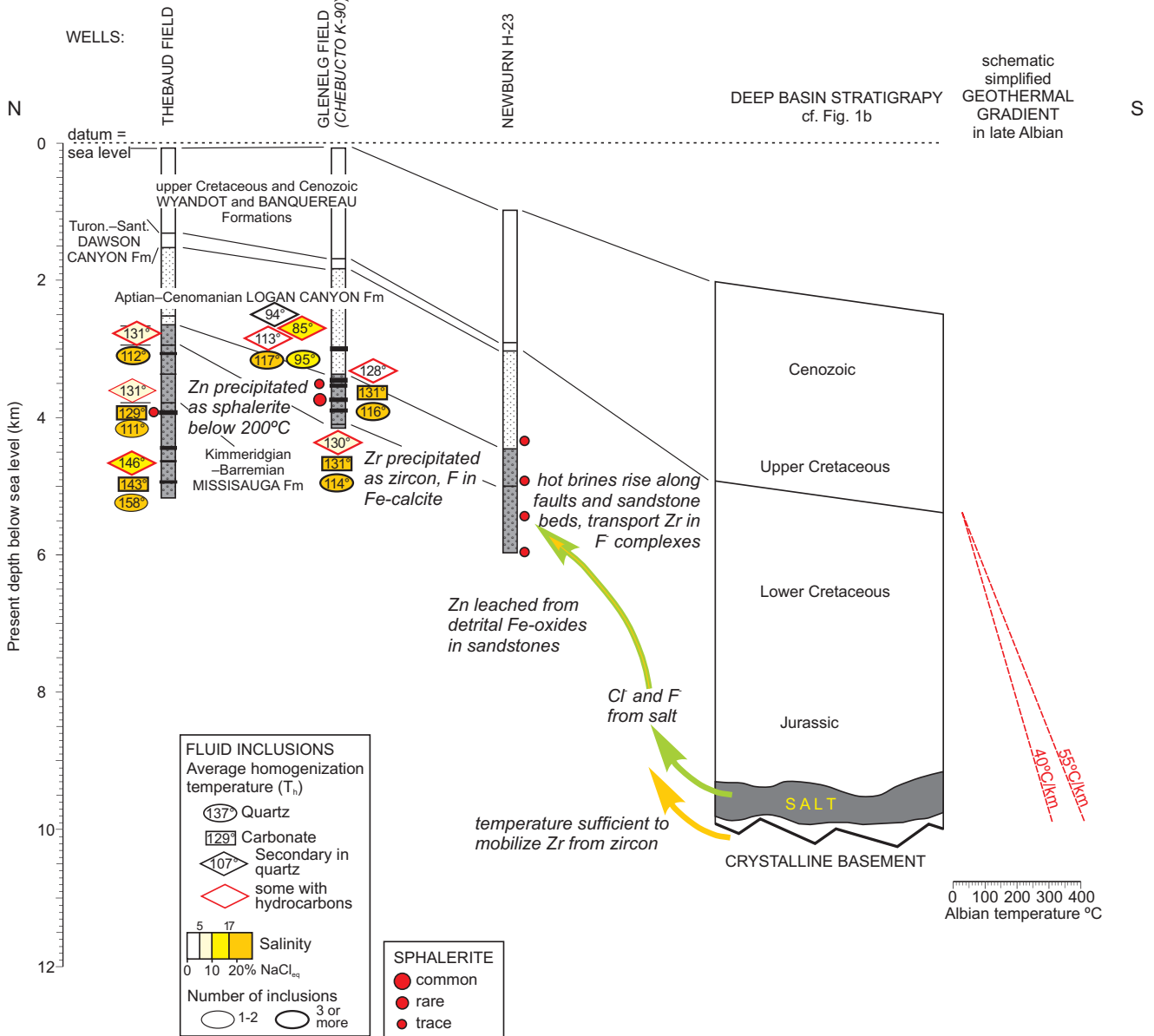


Figure 12